

Surface-Guided Templating of Particle Assemblies Inside Drying Sessile Droplets[†]

Daniel M. Kuncicky and Orlin D. Velev*

Department of Chemical and Biomolecular Engineering, North Carolina State University,
Raleigh, North Carolina 27695-7905

Received July 16, 2007. In Final Form: September 19, 2007

The particles suspended inside evaporating sessile droplets can be assembled into microscopic objects with long-ranged ordered structure. The air–water droplet interface guides the assembly and determines the shape of the resulting micropatches. We report the results of a systematic study of the mechanism of interface-templated assembly on substrates of controlled contact angle. The kinetics of drying were examined by measurements of droplet profiles, and it was found that the rate matched diffusion-limited evaporation well. The shape of the droplets and of the resulting assemblies was correlated to the dynamics of the receding contact line. The effects of major parameters controlling the process, including contact angle, particle concentration, and electrolyte, were investigated in detail. A variety of micropatch shapes were observed and categorized within the parameter space. The in-depth characterization of the process allowed the optimization of the assembly and the formulation of protocols for the deposition of nanostructured patches of different diameter, thickness, and shape.

1. Introduction

The ability to fabricate miniature particle assemblies controllably from organic and inorganic particles could benefit a wide breadth of research and technology areas. Such assemblies may find applications in microassay chip manufacturing,^{1,2} miniaturized photonic band gap materials,³ ink jet printing,^{4,5} and biomechanical probes for the characterization of cells and tissue.⁶ Micrometer- to millimeter-sized 2-D and 3-D arrays of colloidal particles have been fabricated by assembly in confined geometries,^{7–10} capillary flow- and evaporative flux-driven assembly on patterned surfaces,^{11–13} ink jet printing,¹⁴ nanomanipulation,¹⁵ and dielectrophoresis.¹⁶ The electro-optical, mechanical, and chemical functionality of such materials is derived not only from the internal particle organization but also from the overall shape and homogeneity of the micropatch.

The drying of a sessile drop of a colloidal suspension on a surface is seemingly a simple fabrication strategy because no complex equipment or microfabrication steps are required. As

the droplet dries, the meniscus serves as a template and directs the formation of the resulting colloidal crystal. The mechanism of particle assembly, however, turns out to vary strongly depending on the dynamics of the receding contact line.^{17,18} Hence, controlling the shape and quality of the colloidal crystal formed inside the droplets can be quite arduous. Two distinctive droplet drying modes have been described in the literature. The droplets could dry with a constant contact area and decreasing contact angle or with a constant contact angle with decreasing contact area.¹⁹ The constant contact area mode with a pinned contact line is commonly observed on hydrophilic surfaces. The particles could contribute to pinning by jamming into the wedge region near the contact line.^{20,21} Formation of uniform micropatches is usually hindered as the particles are typically transported to the periphery to compensate for the loss of solvent due to evaporation, forming ringlike deposits.^{17,18,22–24}

The constant contact angle drying mode is commonly observed on partially wettable surfaces. On such hydrophobic surfaces, the line recedes during much of the drying process. The particles crystallize as the free volume is reduced with evaporation. The resulting colloidal crystal micropatch can take the form of a spherical cap with geometry dictated by the receding contact angle. Particle assemblies deposited by sessile droplet templating are shown in Figure 1, illustrating the effect of the two distinctive modes of evaporation on final micropatch architecture.

Deegan et al. formulated a theoretical basis for describing the convective flow responsible for particle transport in the drying sessile drops with a pinned contact line.¹⁸ Their analysis showed that during evaporation the meniscus flattens, causing an outward flux of solvent toward the periphery. Hu and Larson²⁵ improved

[†] Part of the Molecular and Surface Forces special issue.

* Corresponding author. E-mail: odvelev@unity.ncsu.edu. Phone: 919-513-4318. Fax: 919-515-3465.

- (1) Blosssey, R.; Bosio, A. *Langmuir* **2002**, *18*, 2952–2954.
- (2) Dugas, V.; Broutin, J.; Souteyrand, E. *Langmuir* **2005**, *21*, 9130–9136.
- (3) Tsuji, S.; Kawaguchi, H. *Langmuir* **2005**, *21*, 8439–8442.
- (4) Tay, B. Y.; Edirisinghe, M. J. *Proc. R. Soc. London, Ser. A* **2002**, *458*, 2039–2051.
- (5) Ko, H. Y.; Park, J.; Shin, H.; Moon, J. *Chem. Mater.* **2004**, *16*, 4212–4215.
- (6) Kuncicky, D. M.; Bose, K.; Costa, K. D.; Velev, O. D. *Chem. Mater.* **2007**, *19*, 141–143.
- (7) Kim, E.; Xia, Y. N.; Whitesides, G. M. *Adv. Mater.* **1996**, *8*, 245–247.
- (8) Velev, O. D.; Furusawa, K.; Nagayama, K. *Langmuir* **1996**, *12*, 2374–2384.
- (9) Dinsmore, A. D.; Hsu, M. F.; Nikolaides, M. G.; Marquez, M.; Bausch, A. R.; Weitz, D. A. *Science* **2002**, *298*, 1006–1009.
- (10) Velev, O. D.; Lenhoff, A. M.; Kaler, E. W. *Science* **2000**, *287*, 2240–2243.
- (11) Fan, F. Q.; Stebe, K. J. *Langmuir* **2004**, *20*, 3062–3067.
- (12) Fustin, C. A.; Glasser, G.; Spiess, H. W.; Jonas, U. *Langmuir* **2004**, *20*, 9114–9123.
- (13) Vyawahare, S.; Craig, K. M.; Scherer, A. *Nano Lett.* **2006**, *6*, 271–276.
- (14) Park, J.; Moon, J.; Shin, H.; Wang, D.; Park, M. J. *Colloid Interface Sci.* **2006**, *298*, 713–719.
- (15) Harel, E.; Meltzer, S. E.; Requicha, A. A. G.; Thompson, M. E.; Koel, B. E. *Nano Lett.* **2005**, *5*, 2624–2629.
- (16) Lumsdon, S. O.; Kaler, E. W.; Velev, O. D. *Langmuir* **2004**, *20*, 2108–2116.

- (17) Adachi, E.; Dimitrov, A. S.; Nagayama, K. *Langmuir* **1995**, *11*, 1057–1060.
- (18) Deegan, R. D.; Bakajin, O.; Dupont, T. F.; Huber, G.; Nagel, S. R.; Witten, T. A. *Nature* **1997**, *389*, 827–829.
- (19) Picknett, R. G.; Bexon, R. J. *Colloid Interface Sci.* **1977**, *61*, 336–350.
- (20) Nadkarni, G. D.; Garoff, S. *Europhys. Lett.* **1992**, *20*, 523–528.
- (21) Deegan, R. D. *Phys. Rev. E* **2000**, *61*, 475–485.
- (22) Conway, J.; Korn, H.; Fisch, M. R. *Langmuir* **1997**, *13*, 426–431.
- (23) Fischer, B. J. *Langmuir* **2002**, *18*, 60–67.
- (24) Truskett, V.; Stebe, K. J. *Langmuir* **2003**, *19*, 8271–8279.
- (25) Hu, H.; Larson, R. G. *J. Phys. Chem. B* **2006**, *110*, 7090–7094.

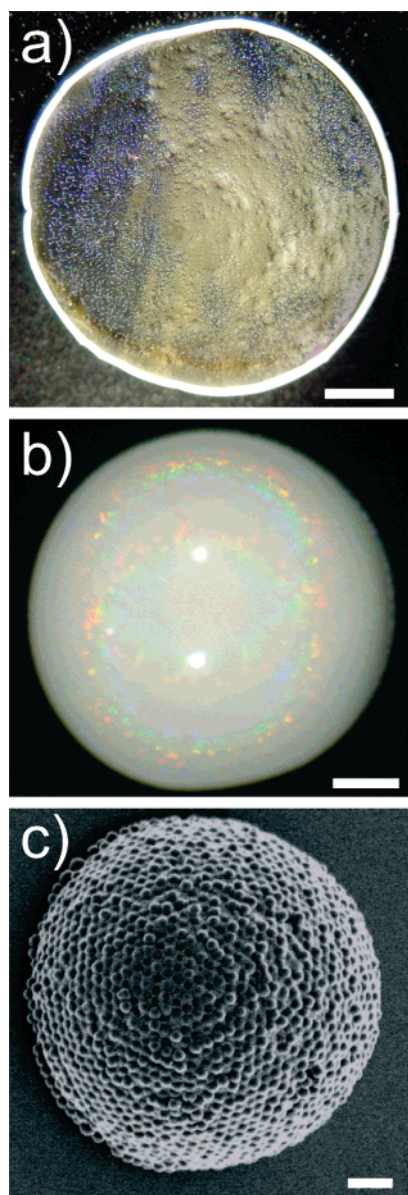


Figure 1. Optical micrographs with examples of the (a) ring stain and (b) spherical cap geometry. The micropatches were deposited by drying microliters of suspension on substrates of controlled wettability. (c) SEM micrograph of a micropatch deposited from nanoliters of suspension. The scale bars in a–c correspond to 0.5 mm, 0.25 mm, and 2 μm .

upon the model of Deegan et al. to include the effects of Marangoni stresses due to thermal gradients along the meniscus surface. The difference in the heat conduction path length across the sessile drops was shown to promote an inward circulatory flow.²⁵ Their experiments proved the connection between circulatory flow patterns and the distribution of particles deposited onto the solid surface. On the basis of this analysis, it has been suggested that staged temperature control could be useful for making uniform coatings by balancing outward convective assembly with temperature-enhanced Marangoni convection to the droplet center.^{25,26} Chang and Velev demonstrated the fabrication of 3-D colloidal crystal structures based on circulation-driven assembly in freely suspended spherical drops.²⁷ Attempts to intricately control the flow in sessile drops have so far proven difficult.

Table 1. Composition and Properties of Substrates Used in the Sessile Droplet Experiments

substrate type	θ_a , degrees	θ_r , degrees	RMS surface roughness, nm
dichlorodimethyl silane	104 ± 1	101 ± 2	5.8
polystyrene	85 ± 2	80 ± 3	5.6
mercaptodecanoic acid	56 ± 5	47 ± 4	6.3
soda lime glass	41 ± 4	32 ± 5	11.3
microscope slide glass	vanishing		9.1

Recently, we reported that high contact angles are a necessary but not sufficient condition for maintaining the hemispherical shape of the meniscus during drying. The final form also depends on the initial particle concentration.⁶ Here, we explore in depth the factors for the interface-driven assembly of colloidal crystal micropatches in drying sessile droplets. We present strategies for control of the shape, uniformity, and particle distribution in the patches by the judicious choice of contact angle and initial particle concentration. The model system is an aqueous suspension of charge-stabilized polystyrene (PS) microspheres. The understanding gained from this research could be beneficial to a variety of technological applications and research areas that involve the deposition of nonvolatile components from evaporating droplets.

2. Materials and Methods

2.1. Colloidal Suspensions and Substrates. Sulfate-stabilized polystyrene latex microspheres (IDC, Portland, OR) were obtained at ~ 8 wt %. The microsphere diameter was 600 nm unless otherwise specified. According to the product data sheet, the surface charge density of sulfate groups was between 2.8 and 3.1 $\mu\text{C cm}^{-2}$. The variation in particle diameter was between 2 and 3% depending on the batch. Residual contaminants and preservatives were removed by gentle centrifugation, followed by replacing of the supernatant with ultrapure deionized (DI) water obtained from a Millipore RiOs 16 system. The washing process was repeated four times prior to the experiments and was found to be critical to obtaining reproducible data. Citrate-stabilized gold nanoparticles with an average diameter of ~ 15 nm were synthesized to yield a concentration of $\sim 6 \times 10^{-3}$ wt % using a well-known protocol.²⁸ Prior to use, the Au nanoparticle suspension was concentrated to ~ 0.6 wt % and washed with DI water using Centricon Plus-20 centrifugal filter units (Millipore, Billerica, MA). In the final step, the gold suspension was concentrated to ~ 5 wt % by sedimentation in a microcentrifuge.

The substrates used for the drying experiments were chosen to cover a broad range of contact angles from 4 to 101° . Glass microscope slides were found to be convenient as highly hydrophilic substrates after chemical treatment of the surfaces. The microscope slides (Fisher Scientific, PA) were first cleaned in Nochromix (Godax Laboratories, MD) overnight, thoroughly rinsed with deionized water from a Millipore RiOs 16 system, and oven dried at 70°C . This process yielded surfaces with vanishing contact angles. Cleaned slides were then exposed to dichlorodimethylsilane vapors (Sigma-Aldrich) in a closed chamber for 15 min at 25°C to yield a hydrophobic surface with a receding contact angle of $\theta_r = 101^\circ$. To prepare a hydrophilic surface with $\theta_r = 47^\circ$, first a layer of 10 nm chromium followed by 90 nm gold was deposited by thermal evaporation onto the glass slide. Then the gold-coated surface was submerged in a 1 mg mL^{-1} ethanol solution of mercaptodecanoic acid (Sigma-Aldrich) in a sealed container for 12 h. Polystyrene slides (Fisher Scientific) served as a moderately hydrophobic substrate with $\theta_r = 80^\circ$. Soda lime glass plates from a commercial source were cleaned with detergent and thoroughly rinsed to yield a substrate with $\theta_r = 32^\circ$. The advancing, θ_a , and receding contact angles and rms roughness for each substrate tested are listed in Table 1. The rms roughness values were measured with a Nanoscope IIIa AFM.

2.2. Droplet Profile Evolution Measurement. The micropatches were formed by drying sessile droplets of a latex suspension on the

(26) Chon, C. H.; Paik, S.; Tipton, J. B.; Kihm, K. D. *Langmuir* **2007**, *23*, 2953–2960.

(27) Chang, S. T.; Velev, O. D. *Langmuir* **2006**, *22*, 1459–1468.

(28) Slot, J. W.; Geuze, H. J. *Eur. J. Cell Biol.* **1985**, *38*, 87–93.

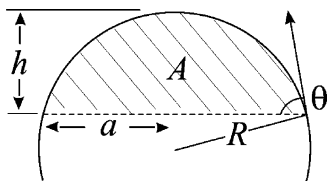


Figure 2. Definition of parameters measured from side profile digital images. On the basis of the spherical cap geometry, any two of these measurables can be used to calculate the droplet volume, V .

substrate surfaces. Unless stated otherwise, $4\ \mu\text{L}$ droplets were used throughout the experiments, and no other solution modifications such as adding surfactant or adjusting pH were made to the suspension. The apparatus was placed in an unsealed box that served to isolate the drop from air currents in the laboratory. The experiments were performed at $22 \pm 1\ ^\circ\text{C}$ and 40–50% relative humidity.

2.3. Data Collection and Analysis. Droplet side profiles were measured with a drop shape analyzer consisting of a level stage, white light source, and 5.0 megapixel Sony DSC-V1 digital camera attached to a microscope head. The microscope head and camera lens allowed for a maximum total visual magnification of up to $60\times$. The white latex suspensions exhibited high contrast against the dark background. Side view photographs were taken at 30 s intervals. The ImageJ 1.36b software package was used to measure the cross-sectional area A , drop height h , contact radius a , and contact angle θ at each time interval from the digital images (Figure 2).

We followed the optical density (transmission) of sessile suspension droplets in the vertical direction in order to characterize the evolution of the particle concentration in the radial direction and the particle stratification near the droplet periphery. Droplets of 0.5 vol % polystyrene microsphere suspension were deposited on transparent polystyrene substrates. A BX61 optical microscope (Olympus, Melville, NY) equipped with a Toshiba PDR-M81 digital camera was used to acquire top view images of drying droplets. The condenser lens was removed from the microscope in order to pass a parallel beam of white light through the bottom of the drying drop. The intensity of the light passed through the drop was recorded at periodic time intervals during the drying process. The grayscale value was measured as a function of radial position on a line 10 pixels wide passing through the center of the drop. The transmission of the light attenuated by the particle suspension was calculated as a function of radial position by normalizing the spatially varying grayscale value with the value measured outside the drop. An extinction coefficient, $\epsilon = 149\ \text{cm}^{-1}$, was experimentally measured for a water suspension of 600 nm polystyrene microspheres using a V550 UV–vis spectrophotometer (Jasco, Japan). Field-emission SEM micrographs were acquired with a JEOL F6400 FESEM at a 5 kV accelerating voltage.

3. Kinetic Equations for the Drying of Sessile Droplets under Diffusion Control

The importance of the sedimentation rate as a function of the microsphere radius, r_p , was determined by gauging the relative magnitude of the thermodynamic versus gravitational forces using the Peclet number, Pe , for sedimentation²⁹

$$Pe = \frac{32\pi r_p^3 \Delta\rho gh}{3kT} \quad (1)$$

Here, $\Delta\rho = (1055 - 998)\ \text{kg m}^{-3}$ is the density difference between water and latex microspheres, g is the gravitational acceleration, k is the Boltzmann constant, and T is the temperature. For 600 nm PS spheres, $Pe \approx 10^2$, and the suspensions do not form packed sediments during the 1 h experiments.²⁹ Using small droplets of suspension also allowed us to simplify data analysis

(29) Russel, W. B.; Saville, D. A.; Schowalter, W. R. *Colloidal Dispersions*; Cambridge University Press: New York, 1989.

by assuming that there is little droplet deformation by gravity. The degree of deformation of the droplets can be evaluated by the dimensionless Bond number, which is the ratio of the surface tension force and the gravitational force

$$Bo = \frac{\rho g R^2}{\gamma} \quad (2)$$

where γ is the surface tension, ρ is the density of water, and R the droplet radius of curvature. For the droplet volumes studied here, $Bo \approx 10^{-1}$. The shape of droplets with Bo of this magnitude can typically be approximated as a spherical cap.

The spherical geometry approximation allows us to specify the position of the air–liquid surface by only two of the variables measured (Figure 2). The “ideality” of the droplet shape was determined experimentally by calculating the value of circularity, C , which is the ratio of the cross-sectional area measured from the digital images to the cross-sectional area for a spherical cap

$$C = \frac{A_{\text{measd}}}{A_{\text{calcd}}} \quad (3)$$

The area A_{calcd} and droplet volume, V , in the spherical segment approximation are easily calculated from two experimentally measured dimensions³⁰

$$A_{\text{calcd}} = \frac{4}{3}ah + \frac{1}{4}\frac{h^3}{a} \quad (4)$$

$$V = \frac{1}{6}\pi h[3a^2 + h^2] = \frac{1}{3}\pi R^3 E$$

$$E = 2 - 3\cos\theta + \cos^3\theta \quad (5)$$

A value of $C = 1$ corresponds to a perfectly spherical cap, and the value decreases commensurate with increased flattening of the droplet. The $4\ \mu\text{L}$ droplets studied in our experiments have $C = 0.99$.

The change in droplet size as a function of evaporation was calculated as follows: for diffusion-controlled evaporation, macroscopic material balance relates the average mass flux, N_e , to droplet volume, V , and the available surface area for evaporation, S .

$$N_e = -\rho \frac{1}{S} \frac{dV}{dt} \quad (6)$$

The vapor concentration, C_w , distribution has been shown to satisfy the Laplace equation

$$\frac{d}{dr}\left(r^2 \frac{dC_w}{dr}\right) = 0 \quad (7)$$

and give a good fit between theory and experiment.^{19,31–41} The

(30) Harris, J. W.; Stocker, H. *Handbook of Mathematics and Computational Science*; Springer-Verlag: New York, 1998.

(31) Fuchs, N. A. In *Evaporation and Droplet Growth in Gaseous Media*; Bradley, R. S., Ed.; Pergamon Press: New York, 1959.

(32) Coutant, R. W.; Penski, E. C. *Ind. Eng. Chem. Fundam.* **1982**, *21*, 250–254.

(33) Birdi, K. S.; Vu, D. T.; Winter, A. *J. Phys. Chem.* **1989**, *93*, 3702–3703.

(34) Rowan, S. M.; Newton, M. I.; McHale, G. *J. Phys. Chem.* **1995**, *99*, 13268–13271.

(35) Bourges-Monnier, C.; Shanahan, M. E. *R. Langmuir* **1995**, *11*, 2820–2829.

(36) Parisse, F.; Allain, C. *Langmuir* **1997**, *13*, 3598–3602.

(37) Erbil, H. Y.; Meric, R. A. *J. Phys. Chem. B* **1997**, *101*, 6867–6873.

(38) Hu, H.; Larson, R. G. *J. Phys. Chem. B* **2002**, *106*, 1334–1344.

(39) Fang, X. H.; Li, B. Q.; Petersen, E.; Ji, Y.; Sokolov, J. C.; Rafailovich, M. H. *J. Phys. Chem. B* **2005**, *109*, 20554–20557.

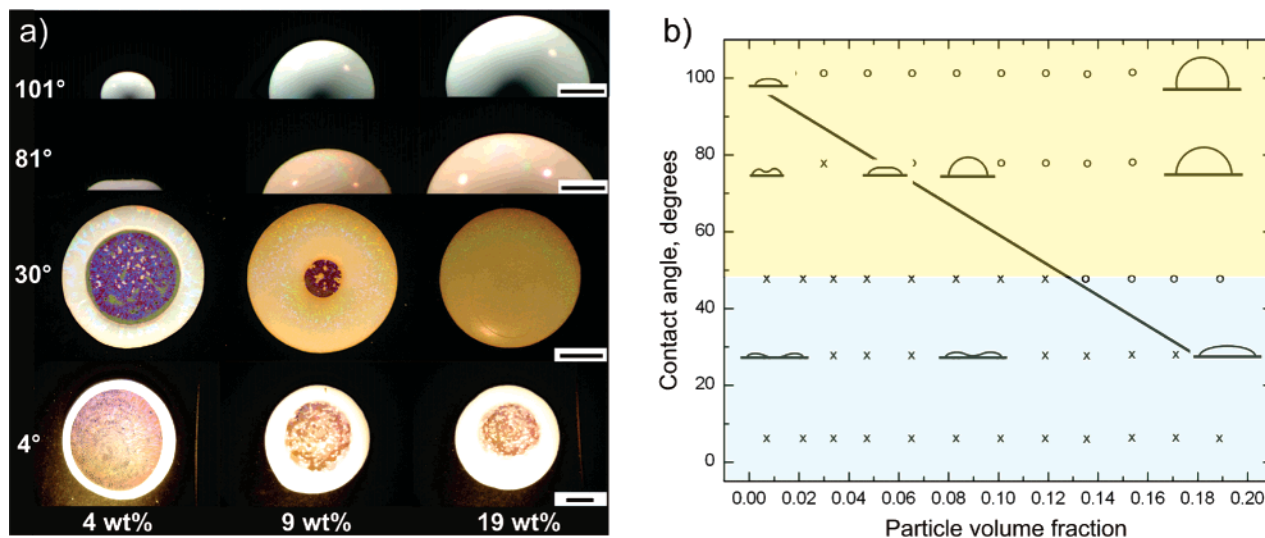


Figure 3. (a) Typical optical images of dried micropatches showing the effect on micropatch shape of varied particle concentration and substrate contact angle. Scale bars from top to bottom: 0.5, 0.5, 1.3, and 2.0 mm. (b) Categorized micropatch shape as a function of θ_r and ϕ_i determined from top and side view optical micrographs. The schematic cross-sectional profiles show how patch architecture varies with volume fraction and contact angle. The open circles (O) are experimental data points corresponding to patches with convex shape, and the crosses (x) are experimental data points corresponding to patches with concave shape. The darker shaded area on the bottom marks the constant contact area drying dynamics. The line to guide the eye shows the predicted edge transition corresponding to the formation of uniform, flat micropatches.

dynamic change in volume can then be related to the diffusivity of water vapor in air, D , and the difference between water vapor concentration by mass at the surface, C_{ws} , and of the ambient air in the room, $C_{w\infty}$ by the following equation:

$$\frac{dV}{dt} = -\frac{4\pi D}{\rho} R(C_{ws} - C_{w\infty}) \quad (8)$$

Equations 7 and 8 assume a spherical drop shape and no substrate present. For sessile droplets on surfaces with intermediate to high contact angles, the calculation of the rate of evaporation requires a geometrical factor, $f(\theta)$, that accounts for the reduced volume available for evaporation due to the substrate. An analytical solution for $f(\theta)$ was derived by Picknett and Bexon,¹⁹ and a good approximation was proposed by Bourges-Monnier et al.^{35,42,43} We obtain the following relation after combining eqs 5 and 8

$$\frac{d}{dt} V^{2/3} = -8 \left(\frac{\pi}{3} \right)^{2/3} K \frac{f(\theta)}{E^{1/3}} \quad (9)$$

$$K = \frac{D(C_{ws} - C_{w\infty})}{\rho}$$

Equation 9 points out that the drying behavior is quite different between the constant contact angle and constant contact area drying modes. Because $f(\theta)$ is constant at fixed contact angle, the analytical solution for $V(t)$ shows a linear $V^{2/3} - t$ decay. However, when the contact area is fixed, $f(\theta)$ decreases concomitant with decreasing contact angle, and no simple analytical solution exists. However, for intermediate contact

angles, the air–liquid surface area changes little for droplets drying in this regime. As a consequence, dV/dt has a weak time dependence and is fairly uniform over the droplet lifetime.^{19,34} The diffusion-limited drying dynamics are used as a basis for comparison with the experimental results and data interpretation. We now present the results of the detailed analysis of the evolution of micropatch formation with the goal of identifying the major parameters that allow for control of the process and the adjustment of micropatch shape, structure, and size.

4. Results and Discussion

4.1. Templating of Latex Colloidal Crystals into Sessile Droplets. **4.1.1. Effect of Particle Concentration and Substrate Contact Angle on Micropatch Shape.** Two classes of dry micropatch shapes were observed. To distinguish between the two, the micropatches with a round, spherical cap shape are denoted “convex”, and those with a ring shape dimpled inward are denoted “concave”. The choice of substrates spanning a broad range of receding contact angles makes it possible to develop a general picture of the effect of contact angle and volume fraction on the process of assembly and final micropatch shape. The side view and top view microscopy images were used to construct an operational phase diagram, which shows the overall shape of the resulting micropatch as a function of θ_r and initial volume fraction ϕ_i (Figure 3).

The results in Figure 3 demonstrate that at any θ_r , the lowering of ϕ_i resulted in the deposition of more particles in the vicinity of the contact line. This process could lead to the formation of the dimpled concave structures. The degree of flattening and the formation of concave structures were more pronounced on substrates with lower contact angles. One interesting and practically important shape that can be formed is patches with a flat top surface. For each contact angle, there is a unique ϕ_i value for the formation of the flat shape, which is between the ϕ_i values giving rise to the convex and concave cases. The line drawn in Figure 3 delineates this transition. Thus, this chart allows for the a priori determination of patch architecture and can be used to pinpoint the conditions for producing uniformly flat micropatches.

(40) McHale, G.; Aqil, S.; Shirtcliffe, N. J.; Newton, M. I.; Erbil, H. Y. *Langmuir* **2005**, *21*, 11053–11060.

(41) Li, G. F.; Butt, H. J.; Graf, K. *Langmuir* **2006**, *22*, 11395–11399.

(42) For ease of use, Picknett and Bexon approximated their exact solution as a polynomial where $f(\theta) = 4.479 \times 10^{-5} + 3.167 \times 10^{-1}\theta + 5.80 \times 10^{-2}\theta^2 - 4.439 \times 10^{-2}\theta^3 + 5.165 \times 10^{-3}\theta^4$ for $0.175 \leq \theta \leq \pi$ radians. The difference from the exact value is reported to be less than 2.0%. Erbil et al. isolated the expression $f(\theta) \approx -\cos \theta/2 \ln(1 - \cos \theta)$ from the Bourges-Monnier and Shanahan solution.

(43) Erbil, H. Y.; McHale, G.; Newton, M. I. *Langmuir* **2002**, *18*, 2636–2641.

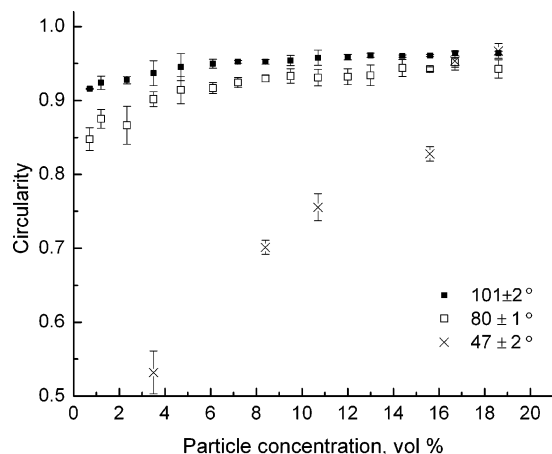


Figure 4. Circularity values calculated from side view optical micrographs such as those from Figure 3a used to quantify how the final shape is correlated to the experimental variables.

The extent of micropatch flattening at the end of the process was quantified by the circularity (eq 3). The average C values from at least 10 dry micropatches at each concentration and for each substrate with $\theta \geq 47^\circ$ are plotted in Figure 4.⁴⁴ These plots show two distinct trends relating C to θ_r .

On the more hydrophilic substrates with $\theta_r = 47^\circ$, the particles in the dry micropatches were deposited in the form of a ring, with the exception of the highly concentrated droplets. C steadily decreased with decreasing ϕ_i . The height and width of the rim around the ring increased with ϕ_i . The drying dynamics were monitored by extracting edge profiles from the side view digital images. An example of a typical edge profile of a droplet deposited on a hydrophilic substrate is shown in Figure 5a. The contact line was pinned throughout the duration of the experiment. This was true for the entire range of ϕ_i studied.

The interface dynamics was quite different on hydrophobic substrates with $\theta \geq 80^\circ$. The shape of the patch and corresponding C value changed very little at medium to high ϕ_i . Micropatches fabricated on the most hydrophobic substrate studied ($\theta_r = 101^\circ$) had $C \approx 0.95$ for $\phi_i \approx 6$ to 20 vol %. Below 6 vol %, the patch flattened with a corresponding decrease in C . The behavior on moderately hydrophobic substrate with $\theta_r = 81^\circ$ was nearly the same. Here, the micropatches had $C \approx 0.92$ for $\phi_i \approx 8$ to 20 vol %, with flattening occurring below 8 vol % particles. Two edge profiles showing the extreme cases for the most dilute and most concentrated suspensions studied are plotted in Figure 5b,c.

The formation of the concave ring structures such as those observed on substrates with $\theta_r \leq 47^\circ$ as a result of contact line pinning is well documented.¹⁸ It has been established that contact line pinning leads to flow-driven particle advection toward the three-phase contact line.¹⁸ In contrast, it is less clear why ϕ_i has such a pronounced influence on the shape of micropatches on hydrophobic substrates where the contact line receded during most of the drying process. To answer this question, we characterized in greater detail the contact line dynamics for droplets drying on poorly wetted substrates.

4.1.2. Relationship between Contact Line Dynamics and Micropatch Shape on Hydrophobic Substrates. We measured the changing contact radius and contact angle for low, intermediate, and high values of ϕ_i . The plots in Figure 6 show three

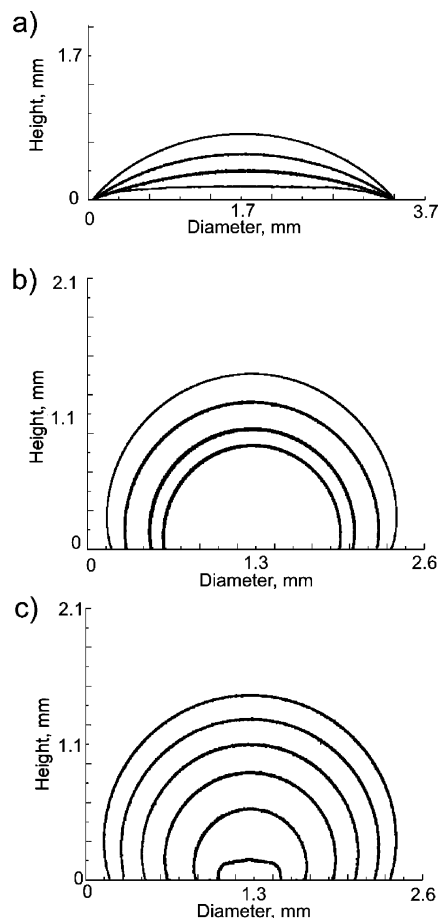


Figure 5. Drying droplet side profile determined from digital images taken at 10 min intervals. The innermost profile corresponds to the final micropatch shape. The parameters for each case are as follows: (a) a 4 μL drop containing 7.0 vol % microspheres, deposited on a hydrophilic substrate with a 47° contact angle, (b) 16 vol %, $\theta_r = 101^\circ$, and (c) 0.25 vol % microspheres, $\theta_r = 101^\circ$. Experiments were conducted at 40% relative humidity and 22°C .

distinct stages during drying. In the first stage, which occurred during the first few minutes, the contact line was pinned as the contact angle concurrently decreased. Such behavior has been well recognized as hysteresis-driven switching from an advancing to a receding contact angle.^{24,45–48} The second stage of drying commenced once the receding contact angle was reached. Here, the line depinned, and the contact area decreased with constant contact angle. We observed a linear time dependence in the contact area and $V^{2/3}$ during constant contact angle drying as predicted by eq 9. The coefficient of correlation values was greater than 0.998. Because the evaporation rate is sensitive to the relative humidity, the slopes of the plots varied slightly with a variation of ca. 5%. Finally, during the last minutes of drying, a third stage commenced. This stage was marked by a repinning of the contact line followed by a slight decrease in θ by up to 10° (see Table 1A in the Supporting Information for detailed results for drying dynamics on hydrophobic substrates). Up until the third stage, the drying droplets had a value of $C \approx 0.99$. Upon repinning of the line, the different micropatch shapes categorized in the phase diagram began to take form.

(44) With the simple drop shape analyzer and camera used, such analysis was not feasible for substrates with $\theta \leq 30^\circ$ because the grayscale typically transitioned from a value of 5 to 250 over ~ 10 pixels at the droplet edge. Because the height of the micropatches deposited on substrates with $\theta < 30^\circ$ was low ($h < 50$ pixels), an accurate determination of the edge transition was not possible. For these cases, the top view images provide a qualitative picture of the concave or convex shape.

(45) de Gennes, P. G. *Rev. Mod. Phys.* **1985**, *57*, 827–863.
(46) Lam, C. N. C.; Wu, R.; Li, D.; Hair, M. L.; Neumann, A. W. *Adv. Colloid Interface Sci.* **2002**, *6*, 169–191.
(47) Soolaman, D. M.; Yu, H. Z. *J. Phys. Chem. B* **2005**, *109*, 17967–17973.
(48) Perry, R. H.; Green, D. W., Eds. *Perry's Chemical Engineers' Handbook*, 6th ed.; McGraw-Hill: New York, 1983.

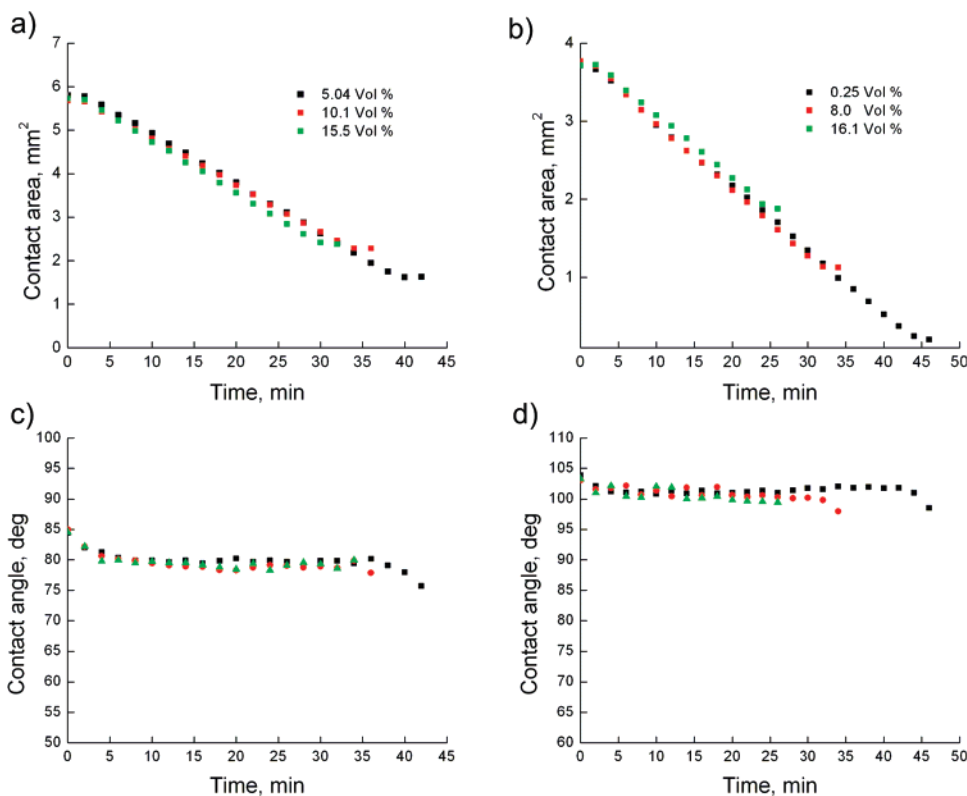


Figure 6. Drying dynamics on (a, c) a moderately hydrophobic surface with $\theta_r = 80^\circ$ and (b, d) a hydrophobic surface with $\theta_r = 101^\circ$. The measurements were taken from edge profiles such as those shown in Figure 5.

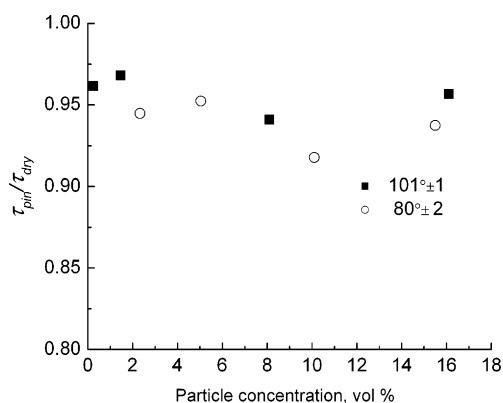


Figure 7. Ratio of contact line pinning time to total drying time as a function ϕ_i and θ_r . The numerical values were determined from Figure 1A in Supporting Information.

An analysis of data from Figure 6a,b (see also Figure 1A in Supporting Information) revealed the surprising fact that the ratio of pinning time to total drying time, $\tau_{\text{pin}}/\tau_{\text{dry}}$, had only a slight, if any, correlation to ϕ_i . The ratio of $\tau_{\text{pin}}/\tau_{\text{dry}}$ was also weakly correlated to the contact angle of hydrophobic substrates and ranged only from ~ 0.96 on the most hydrophobic substrate with $\theta_r = 101^\circ$ to ~ 0.94 for $\theta_r = 80^\circ$ (Figure 7). The lack of strong correlation between ϕ_i and $\tau_{\text{pin}}/\tau_{\text{dry}}$ was counterintuitive because it seemed reasonable that more concentrated suspensions will pin earlier. The discovery that this ratio remains nearly constant allowed us to estimate the particle concentration at the time of pinning, ϕ_{pin} , and correlate it to the final micropatch shape by the numerical procedure presented next.

The particle volume fraction, $\phi(t) \equiv \phi_i(V_i/V(t))$, was calculated from eq 5 using the experimentally measured droplet dimensions.

Table 2. Physical Parameters Used to Calculate the Theoretical Curves in Figure 8

θ_r , degrees	T , °C	P_{satd} , kPa ^a	RH, %	D , cm ² s ⁻¹ ^b	α	β
101	22	2.67	40	0.25	-0.054	2.52

^a From steam tables. ^b Low-density gas diffusion theory.⁴⁸

The following expression for $\phi(t)$ was obtained after integrating eq 9:

$$\phi(t) = \phi_i V_i (\alpha t + \beta)^{-3/2}$$

$$\alpha = -8\{\pi/3\}^{2/3} K \{f/E^{1/3}\} \quad \beta = V_i^{2/3} \quad (10)$$

The physical parameters of evaporation and the numerical values of α and β are listed in Table 2. The analytical results obtained from eq 10 matched the experimental data well (Figure 8). On the basis of this good fit, eq 10 was also used to interpolate between available data points to plot the trends across the entire parameter space.

The results plotted in Figure 8 provide a basis for explaining why ϕ_i has such a profound influence on the micropatch shape on hydrophobic substrates. On the most hydrophobic substrate studied, $\tau_{\text{pin}}/\tau_{\text{dry}} \approx 0.96$ (topmost dashed line in Figure 8). In this case, the volume fraction at pinning, ϕ_{pin} , was near the maximum measured particle concentration of ~ 68 vol % for $\phi_i = 8.0$ to 16.1 vol %. Hence, at medium to high values of ϕ_i , the particle concentration at ϕ_{pin} was near the solidification point. Because there was little volume remaining for particle rearrangement, the convex, nearly spherical shape of the meniscus was maintained until the droplet dried. At low to medium particle concentrations, however, the ϕ_{pin} values precipitously decreased. For the lowest concentration measured, $\phi_i = 0.25$ vol % and $\phi_{\text{pin}} \approx 22$ vol %. Here, the low value of ϕ_{pin} resulted in a flattening of the meniscus

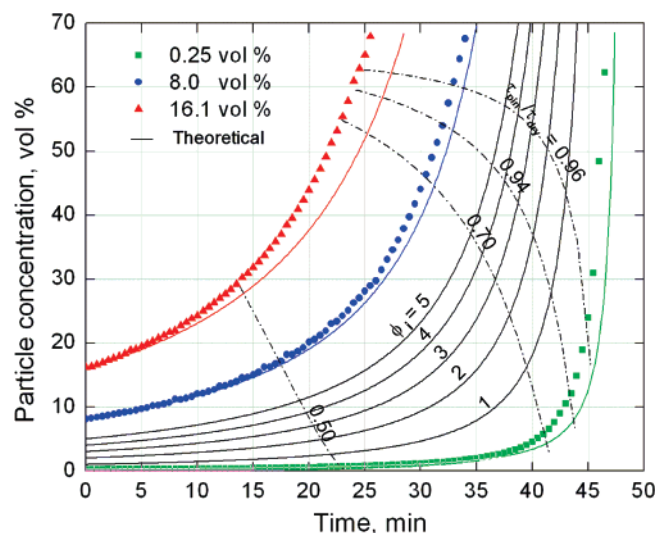


Figure 8. Experimentally measured dynamic change in particle concentration and the interpolated theoretical predictions for $\phi_i = 5, 4, 3, 2$, and 1 vol %. The interpolations are calculated using eq 10 with the parameters from Table 2. The dashed curves indicate where the contact line contraction will stop for different ratios of $\tau_{\text{pin}}/\tau_{\text{dry}}$.

because excess solvent was available for particle transport to the periphery and the formation of ringlike concave structures. This explains the pattern observed at high contact angles in Figure 3. These results provide a framework for controlling the process of sessile droplet assembly on hydrophobic substrates. Conceivably, ϕ_i could be “dialed in” to tune the micropatch shape on substrates with a range of contact angles.

4.1.3. Shell Formation. The mechanism of contact line pinning in the late stages of suspension evaporation is a key to understanding interface-guided assembly. Researchers have suggested that self-pinning can occur because of the formation of a shell of concentrated particles at the meniscus on the basis of experiments performed with polymer solutions^{49,50} and colloidal suspensions^{51–53} with a gelation point. During drying, the shrinking meniscus can collect and concentrate the nonvolatile component at the air–water interface faster than diffusive or circulation-driven mass transport rehomogenizes the drop. The system of PS microspheres studied here is different from previous systems studied in that it does not have a true gelation point and hence the stresses that build up in the shell are likely much weaker. This difference may account for the observed pinning in the very late stages of drying when the shell would be the thickest.

To test for the presence of a particle shell adjacent to the droplet surface in our system, we measured the attenuation of collimated white light passed through the bottom of the drops. We then calculated the theoretical transmission efficiency by assuming the common exponential decay of the light source as a function of path length:

$$T = \exp[-\epsilon(\phi_s l_s(t) + \phi_i l(t))] \quad (11)$$

(49) Gorand, Y.; Pauchard, L.; Calligari, G.; Hulin, J. P.; Allain, C. *Langmuir* **2004**, *20*, 5138–5140.

(50) Kajiya, T.; Nishitani, E.; Yamaue, T.; Doi, M. *Phys. Rev. E* **2006**, *73*, 011601.

(51) Pauchard, L.; Parris, F.; Allain, C. *Phys. Rev. E* **1999**, *59*, 3737–3740.
(52) Tsapis, N.; Dufresne, E. R.; Sinha, S. S.; Riera, C. S.; Hutchinson, J. W.; Mahadevan, L.; Weitz, D. A. *Phys. Rev. Lett.* **2005**, *94*, 018302.

(53) Sugiyama, Y.; Larsen, R. J.; Kim, J. W.; Weitz, D. A. *Langmuir* **2006**, *22*, 6024–6030.

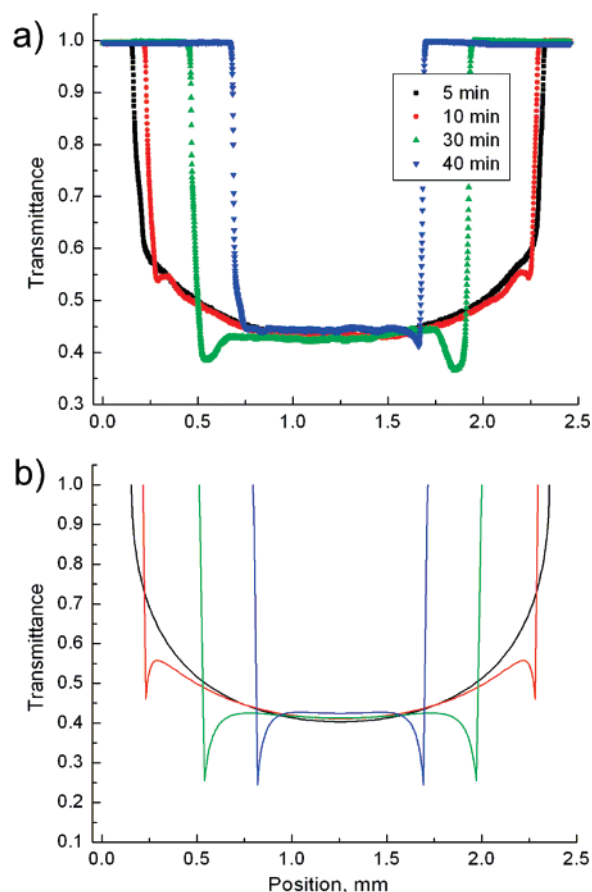


Figure 9. (a) Experimental and (b) theoretical transmittance plots used to identify the formation of a thin shell at the air–water interface during drying. The experiment was performed with $\phi_i = 0.5$ vol % onto a polystyrene substrate with $\theta_c = 80^\circ$.

We assumed a shell concentration of $\phi_s = 0.6$ and a bulk concentration equal to the initial concentration ϕ_i . The experimentally measured contact radius was used to calculate the shell thickness from a material balance similar to those in other reports.⁵² The shell thickness was related to the shell path length, l_s , and the bulk path length, l , based on the spherical cap approximation. The results are plotted in Figure 9. The shape similarity and reasonably good quantitative agreement between the experimental results at short times where the observation of the particle distribution is clearer and there is a calculated profile prove that a shell from concentrated particles is formed near the droplet interface during drying.

4.1.4. Effect of Electrolyte on the Process of Meniscus Templating. The results described in the previous section prove that shell formation is critical in the pinning of the contact line. Because adding electrolyte decreases the electrostatic repulsion between charged latexes, it could be expected to be a major factor in modulating the kinetics of interfacial templating. We systematically varied the ionic strength of the sessile droplet suspension with the goal of correlating the particle–particle and particle–substrate adhesion to the drying dynamics and corresponding micropatch shape. In the range of KCl concentrations studied, the surface tension and evaporation rate have negligible deviations from those of deionized water. As a control, ϕ_i and θ_c were kept constant.

Two series of observations were made regarding the effect of KCl on micropatch structure and assembly based on optical micrographs such as those shown in Figure 10. First, from the images of droplets washed away after 5 min of drying to reveal the layer of particles stuck on the surface, we observed an increase

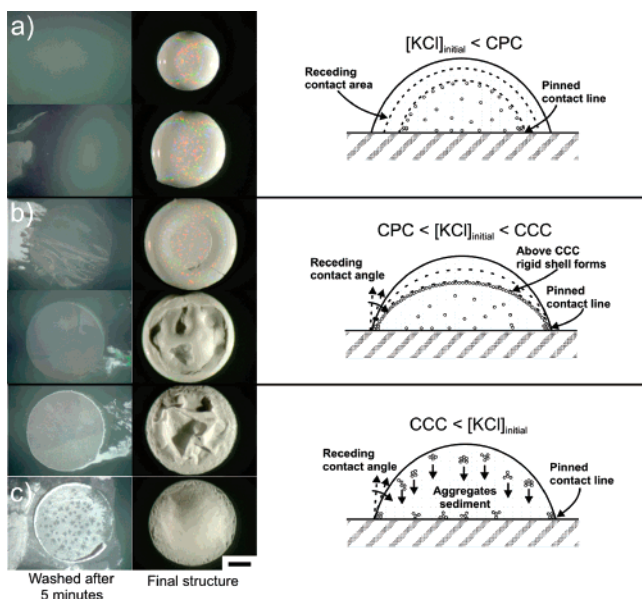


Figure 10. Dried micropatches deposited from suspensions of 7 wt % PS microspheres on a substrate with $\theta_r = 80^\circ$ at 22 °C and 50% relative humidity. The initial concentrations of KCl (from top to bottom) were 0.02, 0.17, 17.0, 67.0, 134, and 168 mM. The images on the left were obtained after droplets had been gently rinsed away with deionized water 5 min after the start of the experiment. The schematics show the proposed mechanism of assembly corresponding to electrolyte concentration (a) below the critical pinning concentration (CPC), (b) in between the CPC and the critical coagulation concentration (CCC), and (c) above the CCC. The scale bar is 0.6 mm.

in the number of particles adhered to the substrate with an increase in KCl concentration. The second series of observations is based on the images of the final micropatch. The addition of electrolyte resulted in micropatches that had a larger diameter with a flattened or slightly concave structure. The drying dynamics can now be categorized into three distinct regimes demarcated by the critical pinning concentration (CPC) and the critical coagulation concentration (CCC) of electrolyte (Figure 10).

The first regime, illustrated in Figure 10a, occurred when the KCl concentration was less than 17 mM. The initial drying pattern was typical of that observed on hydrophobic substrates. The contact line, however, pinned earlier than in droplets of pure water. Because the KCl concentration increased during drying, we hypothesize that at this moment the increasing electrolyte concentration reached the CPC. At the CPC, the particles adhered to the substrate in sufficient amounts to cause contact line pinning. On the basis of the volume change of the droplet, we calculated the average KCl concentration in the droplet at periodic intervals. By correlating τ_{pin} to the change in KCl concentration, we identified a narrow range for the CPC between 4.6 and 5.8 mM (Figure 11).

The second regime, shown in Figure 10b, occurred when the initial KCl concentration was greater than the CPC. The contact line was pinned throughout the duration of the experiment. If the initial KCl concentration was between 67 and 168 mM, then the particles adjacent to the air–water interface coagulated and formed a rigid shell. Ultimately, the shell crumpled as the meniscus continued to shrink. We hypothesize that the shell formed because the KCl concentration near the surface reached the CCC before most of the solvent had evaporated. The local increase in electrolyte concentration could result in particle coagulation in the thin shell earlier than coagulation in the bulk.

The third regime, shown in Figure 10c, occurred when the initial KCL concentration was near the CCC. Studies of similar

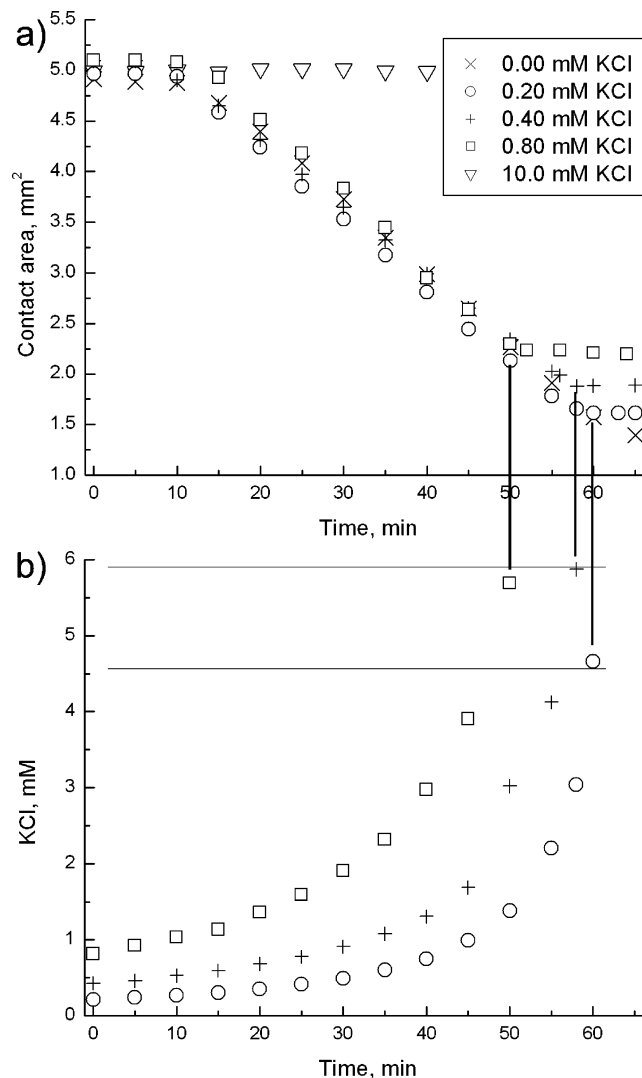


Figure 11. (a) Dynamic change in contact area related to (b) the average KCl concentration in the shrinking drop. The point of contact line pinning is indicated by the break in the contact area plots. The vertical lines highlight this break to demarcate the KCl concentration at τ_{pin} for identification of the critical pinning concentration.

microspheres suggest that the CCC is on the order of 200 mM.⁵⁴ In our experiments, adding 168 mM KCl caused the PS microspheres to aggregate and sediment out of solution within the time frame of the 1 h experiment. As the droplet continued to dry, the “sand pile” structure shown in the optical micrograph was formed.

The existence of two critical electrolyte concentrations (Figures 10 and 11) along with the observation of particle adhesion to the substrate and aggregation on the surface can be explained by the suppression of the electrostatic repulsion by electrolyte screening. We estimated the threshold of particle adherence to the substrate on the basis of the DLVO theory for the balance of attractive van der Waals and repulsive electrostatic potential between a charged sphere and a plate. The energy of interaction was calculated from the linearized Poisson–Boltzmann equation and the Derjaguin approximation:⁵⁵

$$W_{\text{DLVO}} = -\frac{A_H r_p}{6d} + 64\pi\epsilon\epsilon_0 r_p \Gamma_s \Gamma_p \left(\frac{k_B T}{e}\right)^2 \ln(1 + e^{-\kappa d}) \quad (12)$$

(54) Bergendahl, J.; Grasso, D. *AIChE J.* **1999**, *45*, 475–484.

(55) Verwey, E. J.; Overbeek, J. T. G. *Theory of the Stability of Lyophobic Colloids*; Elsevier: Amsterdam, 1948.

In eq 12, subscripts s and p refer to sphere and plate, κ is the inverse Debye screening length, $A_H = 1.4 \times 10^{-20}$ J is the Hamaker constant based on Lifshitz theory,⁵⁶ d is the distance between surfaces, $\Gamma = \tanh(e\psi/4k_B T)$, ϵ is the dielectric constant, e is the electron charge, and ψ is the surface potential for a sphere or plate. On the basis of the surface charge density reported for the particles and electrophoretic mobility experiments, ψ_s is in the range of 80–100 mV, and ψ_p is in the range of 20–50 mV.⁵⁷ By applying the criteria for colloidal stability ($W = dW/dD = 0$) to eq 12, we estimated a critical KCl concentration of ~ 80 mM for particle–substrate coagulation. This value is an order of magnitude higher than the one measured from Figure 11. The first reason for this discrepancy could be the presence of strong hydrophobic attraction. Studies based on atomic force microscopy (AFM) and flow cell detachment suggest that long-range hydrophobic attractive interactions can be a major contribution to the interaction potential between particles and flat surfaces.^{58,59} Similar studies have also shown that the work of adhesion required to separate hydrophobic surfaces increases with electrolyte concentration.⁶⁰

The second reason for DLVO theory overevaluating the electrolyte CPC can be the evaporation-driven concentration of electrolyte near the contact line. As already pointed out, evaporation can concentrate electrolytes at the meniscus if the evaporation flux is larger than the diffusive mass flux toward the bulk. Furthermore, Deegan et al.²¹ have shown that the evaporation rate is highest near the three-phase contact line. At this point, it is difficult to draw definitive conclusions on the exact mechanism for particle–substrate adhesion. Nevertheless, the finding that electrolyte concentration could trigger strong contact line pinning through the CPC and CCC could have consequences in a variety of technologies where electrolyte is present or could be used as an additional operational parameter for controlling droplet shape. One such area is DNA microarray technology where ring stains commonly form around droplets from buffered biological samples and complicate data acquisition.

4.2. Materials Applications: The Deposition of “Inverse Opal” Gold Nanoparticle Micropatches. Micropatches of controlled shape and structure assembled from colloid spheres could have important applications in technology. The results described in the previous sections reveal the means to control the shape of micropatches by controlling the surface shape and particle interactions. One structure of particular importance could be circular patches with a flat top surface. These patches can be used, for example, in sensors based on surface-enhanced Raman scattering (SERS). In our earlier work, we demonstrated how crystals of polystyrene microspheres can serve as a template for the assembly of gold nanoparticles into structured porous films and stripes ranging from millimeters to centimeters.^{61,62} Further miniaturization of the SERS materials could prove beneficial for sampling in microfluidic chambers, which can have volumes as small as a few picoliters, and also for making arrays of patches analogous to the presently used parallel bioassays.

The technique developed was adapted for making porous gold nanoparticle micropatches. The assembly was carried out by

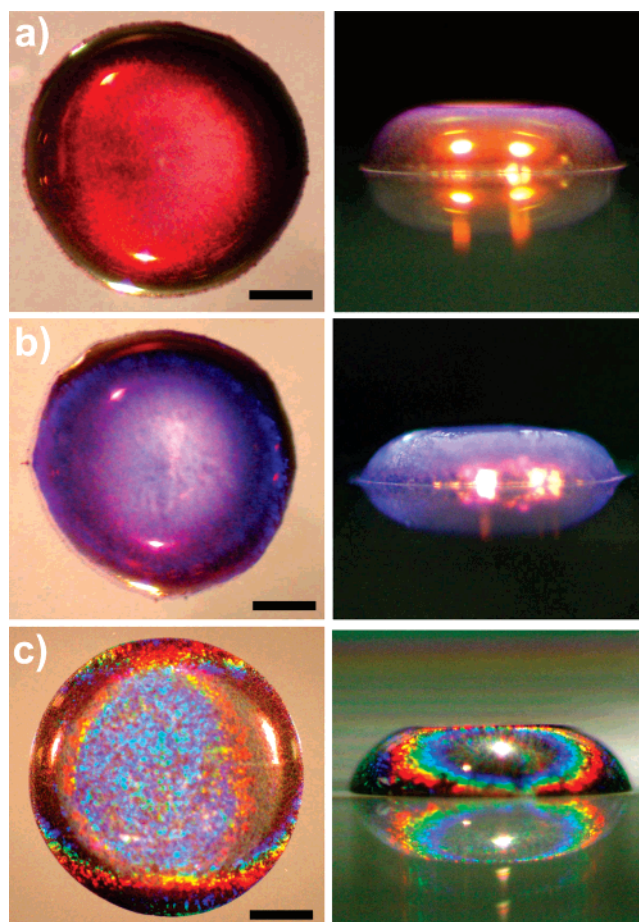


Figure 12. Optical micrographs of micropatches made from a mixture of gold nanoparticles and (a) 250, (b) 300, and (c) 600 nm PS microspheres. Experimental conditions were 2:1 5 wt % Au/16 vol % PS, $\theta_r = 101^\circ$. The scale bars corresponds to 0.3 mm.

depositing a mixture of ~ 15 nm, 5 wt % Au nanoparticles and 16 vol % PS microspheres. Both particle types have a negative surface charge and are stable when mixed. We observed the same general effects of ϕ_i and θ_r on micropatch shape and circularity as for deposition with PS spheres only. The only deviation in the presence of gold nanoparticles was a slight reduction in $\tau_{\text{pin}}/\tau_{\text{dry}}$. Such similarity in drying behavior allowed for the control of micropatch shape with only minor modifications to the deposition conditions categorized in Figure 3.

Examples of flat, uniformly shaped micropatches are shown in Figure 12. The lattice spacing of particles in the 3-D micropatches fabricated here is on the order of visible light and results in coloring due to Bragg diffraction. The colors of the micropatches were dependent on the templating sphere diameter and the scattering angle of observation (Figure 12).

Observation of the microstructure using SEM revealed that the micropatches were polycrystalline with grain boundaries separating domains of crystallized particles with triangular close-packed symmetry. The rainbow of colors in Figure 12c arises because the polycrystalline scattering planes are aligned in multiple directions along these grain boundaries. The opalescence of micropatches fabricated from PS microspheres only (Figure 1b) was less brilliant than with gold nanoparticles added (Figure 12). This effect is most likely due to the higher reflectivity of the gold nanoparticles.

The concentration of gold nanoparticles in the droplets also affected the overall quality of the crystal structure. In a typical experiment, the concentration of gold nanoparticles was not

(56) Evans, F. D.; Wennerstrom, H. *The Colloidal Domain Where Physics, Chemistry, Biology, and Technology Meet*; Wiley-VCH: New York, 1999.

(57) Sousa, M.; Azeredo, J.; Feijo, J.; Oliveira, R. *Biotechnol. Tech.* **1997**, *11*, 751–754.

(58) Freitas, A. M.; Sharma, M. M. *Langmuir* **1999**, *15*, 2466–2476.

(59) Freitas, A. M.; Sharma, M. M. *J. Colloid Interface Sci.* **2001**, *233*, 73–82.

(60) Kokkoli, E.; Zukoski, C. F. *Langmuir* **1998**, *14*, 1189–1195.

(61) Kuncicky, D. M.; Christesen, S. D.; Velev, O. D. *Appl. Spectrosc.* **2005**, *59*, 401–409.

(62) Kuncicky, D. M.; Prevo, B. G.; Velev, O. D. *J. Mater. Chem.* **2006**, *16*, 1207–1211.

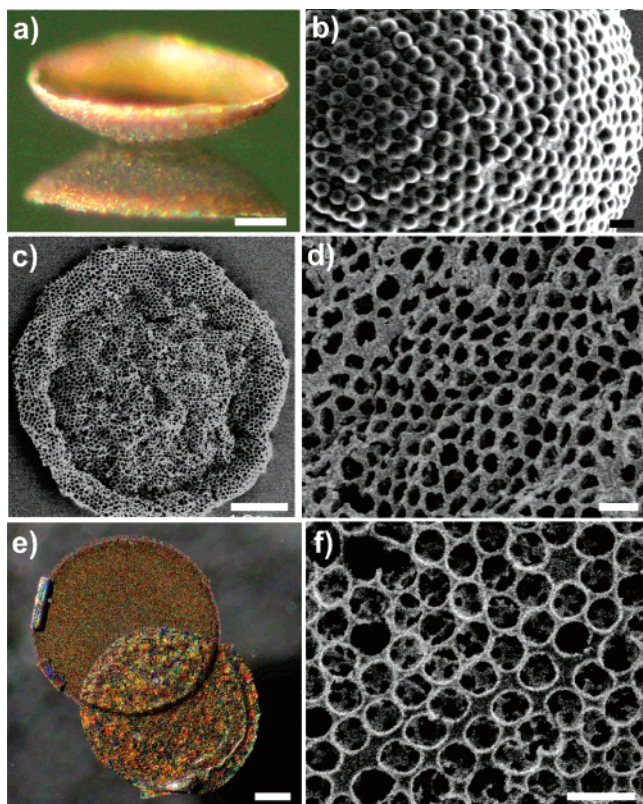


Figure 13. Typical microstructures formed from a mixture of gold nanoparticles and PS microspheres: (a) optical and (b) corresponding SEM micrograph of the lens structure shows inner curvature and the arrangement of gold nanoparticles aggregated around PS microspheres. (c, d) SEM micrographs of the lens in a and b after heating in air to remove the PS microspheres. (e) Optical and (f) SEM micrograph of the micropatch from Figure 12c after dissolving the polymer component in methylene chloride. The scale bars for a–f correspond to 10, 1, 10, and 1 μm , 0.4 mm, and 1 μm .

sufficient to fill the interstitial space between the crystallized PS microspheres entirely. Interestingly, we found that the gold nanoparticles stratify on the top and bottom parts of the patches. Evidence for the stratification of the mixture during drying is shown in Figure 13e, where the dried patch was submerged in methylene chloride for 10 min to dissolve the PS component. The reasons for this stratification will be investigated in our future work.

We earlier showed that the patches composed of PS microspheres are robust and stable.⁶ The round micropatches with a spherical cap shape assembled here could be peeled off of the

substrate and submerged in water without disrupting the structure. The principles of assembly in sessile droplets applied over a broad range of droplet volumes from 0.1 nL to 4 μL , thereby allowing for scaling down the process and the fabrication of micropatches with diameter ranging from micrometers to millimeters. One particularly interesting result was observed with Au/PS mixtures deposited from nanoliter volumes of suspension. These micropatches of diameter smaller than 100 μm had a characteristic lens-type structure (Figure 13a). The templating PS spheres could be removed by heating in air at 450 $^{\circ}\text{C}$ for 5 min; however, SEM micrographs revealed that the porous lens structure flattened after heating (Figure 13c,d).

5. Conclusions

This work categorizes the micropatch shape resulting from templating by the liquid surface as a result of a few controlling parameters: contact angle, particle concentration, and electrolyte concentration. The use of hydrophobic substrates was shown to be a necessary but not sufficient condition for avoiding “coffee ring” formation. By monitoring the kinetics of drying from side profile images, we showed that droplets of low initial particle concentration were more likely to flatten and deform when contact line pinning occurred during the late stages of drying. This result was interpreted in terms of diffusion-limited drying dynamics. The analysis showed that droplets of low initial particle concentration had only a small change in free volume during most of the drying process until the last few minutes of drying. A transmitted light attenuation experiment provided evidence that a thin shell of particles formed at the air–water interface during drying. The shell is known to increase the local viscosity near the interface in other multicomponent mixtures and may be the cause of self-pinning. A critical electrolyte concentration was identified, which was shown to correlate to contact line pinning and particle substrate adhesion. The trends outlined could have a broad application for controlling the architecture of particle assemblies deposited from drying sessile droplets of suspension on surfaces of controlled wettability.

Acknowledgment. We are grateful to John van Zanten for insightful and useful discussions. This study was supported by grants from the Air Force Research Office and the NIH.

Supporting Information Available: Numerical values measured from the drying dynamics plots and magnified plots highlighting the point of transition to a pinned contact line. This material is available free of charge via the Internet at <http://pubs.acs.org>.

LA702129B